Magnetization and energy dynamics in spin ladders: Evidence of diffusion in time, frequency, position, and momentum

Jonas Richter, Fengping Jin, Lars Knipschild, Jacek Herbrych, Hans De Raedt, Kristel Michielsen, Jochen Gemmer, and Robin Steinigeweg

Phys. Rev. B **99**, 144422 — Published 23 April 2019

DOI: 10.1103/PhysRevB.99.144422

Magnetization and energy dynamics in spin ladders: Evidence of diffusion in time, frequency, position, and momentum

Jonas Richter,[1,*] Fengping Jin,[2] Lars Knipschild,[1] Jacek Herbrych,[3,4] Hans De Raedt,[5] Kristel Michielsen,[2,6] Jochen Gemmer,[1] and Robin Steinigeweg[1,†]

[1] *Department of Physics, University of Osnabrück, D-49069 Osnabrück, Germany*
[2] *Institute for Advanced Simulation, Jülich Supercomputing Centre, Forschungszentrum Jülich, D-52425 Jülich, Germany*
[3] *Department of Physics and Astronomy, The University of Tennessee, Knoxville, Tennessee 37996, USA*
[4] *Materials Science and Technology Division, Oak Ridge National Laboratory, Oak Ridge, Tennessee 37831, USA*
[5] *Zernike Institute for Advanced Materials, University of Groningen, NL-9747AG Groningen, The Netherlands*
[6] *RWTH Aachen University, D-52056 Aachen, Germany*

(Dated: February 15, 2019)

The dynamics of magnetization and energy densities are studied in the two-leg spin-1/2 ladder. Using an efficient pure-state approach based on the concept of typicality, we calculate spatio-temporal correlation functions for large systems with up to 40 lattice sites. In addition, two subsequent Fourier transforms from real to momentum space as well as from time to frequency domain yield the respective dynamical structure factors. Summarizing our main results, we unveil the existence of genuine diffusion both for spin and energy. In particular, this finding is based on four distinct signatures which can all be equally well detected: (i) Gaussian density profiles, (ii) time-independent diffusion coefficients, (iii) exponentially decaying density modes, and (iv) Lorentzian line shapes of the dynamical structure factor. The combination of (i) - (iv) provides a comprehensive picture of high-temperature dynamics in this archetypal nonintegrable quantum model.

I. INTRODUCTION

The study of low-dimensional spin systems is one of the most active fields in condensed matter physics. On the one hand, quantum spin models are of immediate relevance to describe the properties of various Mott insulators, where (quasi) one-dimensional structures like chains or ladders are realized within the bulk materials. The notion of property can be manifold in this context, including thermodynamic quantities [1], transport characteristics such as the heat conductivity [2, 3], as well as other dynamic features probed by, e.g., neutron scattering [4, 5], NMR [6], and μSR [7], to name just a few. Particularly, developing a thorough understanding of quantum magnets, both experimentally and theoretically, is also of essential importance in order to pave the way for potential spin-based technologies in the future [8].

On the other hand, from a more fundamental point of view, low-dimensional spin models represent prototypical examples of interacting quantum many-body systems, allowing to study questions ranging from the foundations of statistical mechanics [9] to the physics of black holes [10]. In particular, long-standing questions concerning the emergence of thermodynamic behavior in isolated quantum systems have recently experienced rejuvenated attention [11–14]. This upsurge of interest is not least due to the advance of controlled experiments with cold atoms and trapped ions [15–17], theoretical key concepts such as the eigenstate thermalization hypothesis [18–21] and the typicality of pure quantum states [22–25], as well as the development of powerful numerical techniques [26].

Concerning the relaxation in isolated quantum systems, an intriguing question is the difference in the properties between integrable and nonintegrable systems. On the one hand, integrable systems exhibit a macroscopic set of (quasi-)local conservation laws [27, 28] which might cause anomalous thermalization [29] as well as nondecaying currents, i.e., ballistic transport [30]. Nonetheless, even for paradigmatic integrable models, signatures of diffusion have been reported, e.g., for the spin-1/2 XXZ chain above the isotropic point [31–36] or the Fermi-Hubbard model for strong particle-particle interactions [37–39]. Moreover, significant progress in understanding transport in integrable models has been recently achieved within the framework of generalized hydrodynamics [40–42]. On the other hand, in more realistic situations, integrability is often lifted due to various perturbations, e.g., spin-phonon coupling [43], long-range interactions [44], dimerization [45], as well as the presence of impurities [46] or disorder [47]. Such nonintegrable systems are commonly expected to have vanishing Drude weights [30] and potentially exhibit diffusive transport, e.g., due to quantum chaos. Notably, the onset of diffusive hydrodynamics under chaotic quantum dynamics has also been substantiated by exact results obtained in random circuit models [48–50]. However, since the dynamics of real interacting systems with many degrees of freedom poses a formidable challenge to theory and numerics, signatures of clean diffusion have been found only for selected examples [34, 51–54].

In this context, we study the dynamics of magnetization and energy in a nonintegrable spin-1/2 system with ladder geometry. In particular, we will demonstrate an

* jonasrichter@uos.de
† rsteinig@uos.de

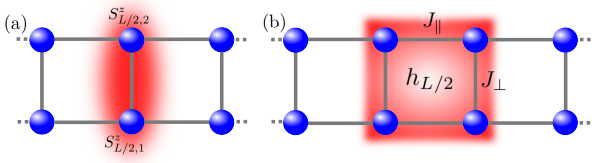

FIG. 1. (Color online) Sketch of the local densities ϱ_l. (a) local magnetization $S^z_{l,1}+S^z_{l,2}$. (b) local energy h_l. Note that h_l is defined with $J_\perp/2$, cf. Eq. (1).

efficient numerical approach based on the concept of typicality [22–25, 55–60], which enables us to study large system sizes and to detect various signatures of diffusive transport.

This paper is structured as follows. We introduce the model in Sec. II and define the observables in Sec. III. In Sec. IV, we outline our numerical approach and present our results in Sec. V. We summarize and conclude in Sec. VI.

II. THE MODEL

The Hamiltonian $\mathcal{H}=\sum_{l=1}^{L} h_l$ of the spin-1/2 ladder with periodic boundary conditions reads

$$h_l = J_{||}\sum_{k=1}^{2}\mathbf{S}_{l,k}\cdot\mathbf{S}_{l+1,k}+\frac{J_\perp}{2}\sum_{n=l}^{l+1}\mathbf{S}_{n,1}\cdot\mathbf{S}_{n,2}\ , \qquad (1)$$

where $\mathbf{S}_\mathbf{r}=(S^x_\mathbf{r},S^y_\mathbf{r},S^z_\mathbf{r})$ are spin-1/2 operators on lattice site $\mathbf{r}=(l,k)$, $J_{||}=1$ denotes the coupling along the legs (and sets the energy scale throughout this paper), and $J_\perp\geq 0$ is the coupling on the L rungs. While for $J_\perp=0$, $\mathcal{H}$ decouples into two separate chains and is integrable in terms of the Bethe ansatz [61], this integrability is broken for any $J_\perp\neq 0$. Numerous works [62–67] have explored the dynamics of the spin ladder (1), also including various modifications such as four-spin terms [68], Kitaev-type couplings [69], as well as XX-ladder systems [70, 71]. However, while these studies often discuss either spin *or* energy transport only, they also mostly focus exclusively on the dynamics of densities *or* currents, either in time *or* in frequency.

In this paper, we do not focus on a particular quantity and representation and provide a comprehensive picture of high-temperature dynamics in the spin-1/2 ladder. As a main result, we unveil the existence of genuine diffusion *both* for magnetization and energy. In particular, this result is based on *the combination of four distinct signatures*: (i) Gaussian density profiles, (ii) time-independent diffusion coefficients, (iii) exponentially decaying density modes, and (iv) Lorentzian line shapes of the dynamical structure factor. We present these signatures for large systems with up to 40 lattice sites.

III. SETUP AND OBSERVABLES

We study the dynamics of time-dependent expectation values

$$p_l(t)=\langle\psi(t)|\,\varrho_l\,|\psi(t)\rangle\ ;\quad \varrho_l=\begin{cases}S^z_{l,1}+S^z_{l,2}\\ h_l\end{cases}\ , \qquad (2)$$

where the time argument has to be understood as $|\psi(t)\rangle=e^{-i\mathcal{H}t}|\psi(0)\rangle$, and the operator ϱ_l denotes the local densities of magnetization or energy (cf. Fig. 1). Furthermore, the (unnormalized) pure initial state $|\psi(0)\rangle$ is prepared as

$$|\psi(0)\rangle=\frac{\sqrt{\tilde{\varrho}_{L/2}}\,|\varphi\rangle}{\sqrt{\langle\varphi|\varphi\rangle}}\ ;\quad |\varphi\rangle=\sum_{k=1}^{d}c_k\,|\varphi_k\rangle\ , \qquad (3)$$

where the complex coefficients c_k are randomly drawn from a Gaussian distribution with zero mean (Haar measure [72]) and the $|\varphi_k\rangle$ denote a set of orthonormal basis states (e.g. the Ising basis) of the full Hilbert space with dimension $d=4^L$. Moreover, the operator $\tilde{\varrho}_{L/2}=\varrho_{L/2}+c$ in Eq. (3) is essentially equivalent to $\varrho_{L/2}$ except for a constant offset which renders the eigenvalues of $\tilde{\varrho}_{L/2}$ nonnegative. Exploiting the concept of dynamical typicality [72, 73], as well as $\mathrm{Tr}[\varrho_l]=0$, the expectation value $p_l(t)$ can be connected to an equilibrium correlation function at formally infinite temperature (see Sec. IV),

$$p_l(t)=\langle\varrho_l(t)\varrho_{L/2}\rangle+\epsilon\ , \qquad (4)$$

with $\langle\cdot\rangle=\mathrm{Tr}[\cdot]/d$. Note that the statistical error $\epsilon=\epsilon(|\varphi\rangle)$ scales as $\epsilon\propto 1/\sqrt{d}$ and is negligibly small for all system sizes studied here [55, 57, 72, 73].

In addition to the spatio-temporal correlation functions (4), the respective correlations in momentum space can be obtained by a lattice Fourier transform [74]

$$p_q(t)=\sum_l e^{iq(l-L/2)}p_l(t)=\langle\varrho_q(t)\varrho_{-q}\rangle\ , \qquad (5)$$

where translational invariance has been exploited, and $\varrho_q=\sqrt{1/L}\sum_l e^{iql}\varrho_l$ with discrete momenta $q=2\pi k/L$ and $k=0,1,\ldots,L-1$. Furthermore, a subsequent Fourier transform from time to frequency domain eventually yields the dynamical structure factor $S(q,\omega)$,

$$p_q(\omega)=\int_{-t_{\max}}^{t_{\max}}e^{i\omega t}p_q(t)\,\mathrm{d}t=S(q,\omega)\ , \qquad (6)$$

with the finite frequency resolution $\delta\omega=\pi/t_{\max}$.

It is further instructive to establish a relation between density dynamics and current-current correlation functions. To this end, let us introduce the time-dependent diffusion coefficient [75]

$$D(t)=\frac{1}{\chi}\int_0^t\frac{\langle j(t')j\rangle}{L}\,\mathrm{d}t'\ , \qquad (7)$$

where $\chi = \lim_{q\to 0}\langle \varrho_q \varrho_{-q}\rangle$ denotes the isothermal susceptibility [76] and the spin- or energy-current operators $j = \sum_l j_l$ follow from a lattice continuity equation $\partial_t \varrho_l = i[\mathcal{H}, \varrho_l] = j_{l-1} - j_l$. More details on current operators and autocorrelation functions are provided in Appendix A. To proceed, we note that the states $|\psi(0)\rangle$ realize an initial density profile $p_l(0)$ which exhibits a δ peak at $l = L/2$ [77]. This initial δ peak will gradually broaden with time and its spatial variance for $t \geq 0$ is given by

$$\sigma(t)^2 = \sum_{l=1}^{L} l^2 \delta p_l(t) - \left(\sum_{l=1}^{L} l \delta p_l(t)\right)^2 , \tag{8}$$

with $\delta p_l(t) = p_l(t)/\sum_l p_l(0)$ and $\sum_l \delta p_l(t) = 1$. Due to the typicality relation in Eq. (4), this variance can be directly connected to the aforementioned diffusion coefficient [78, 79],

$$\frac{\mathrm{d}}{\mathrm{d}t}\sigma(t)^2 = 2D(t) . \tag{9}$$

Note that a diffusive process requires $D(t) = D = \text{const.}$ such that $\sigma(t) \propto \sqrt{t}$ [34], above the mean free time.

IV. NUMERICAL APPROACH

A. Dynamical quantum typicality

First, let us derive the typicality relation given in Eq. (4). To this end, we start with an infinite-temperature correlation function,

$$\mathcal{C}_{l,l'}(t) = \frac{\mathrm{Tr}[\varrho_l(t)\tilde{\varrho}_{l'}]}{d} = \frac{\mathrm{Tr}[\varrho_l(t)\varrho_{l'}] + c\mathrm{Tr}[\varrho_l]}{d} , \tag{10}$$

where $\tilde{\varrho}_{l'} = \varrho_{l'} + c$ has a nonnegative spectrum. We realize that Eq. (10) can be simplified if either $c = 0$ or $\mathrm{Tr}[\varrho_l] = 0$. Focusing on these cases, one finds

$$\mathcal{C}_{l,l'}(t) = \mathrm{Tr}[\varrho_l(t)\varrho_{l'}]/d = \langle \varrho_l(t)\varrho_{l'}\rangle , \tag{11}$$

i.e., the correlation functions $\langle \varrho_l(t)\tilde{\varrho}_{l'}\rangle$ and $\langle \varrho_l(t)\varrho_{l'}\rangle$ are equivalent. This is a first important observation. Furthermore, exploiting the cyclic invariance of the trace, Eq. (10) can be written as

$$\mathcal{C}_{l,l'}(t) = \frac{\mathrm{Tr}[\sqrt{\tilde{\varrho}_{l'}}\varrho_l(t)\sqrt{\tilde{\varrho}_{l'}}]}{d} , \tag{12}$$

where the square root operation has to be understood in a representation where $\tilde{\varrho}_{l'}$ is diagonal (cf. Sec. IV B). Using the concept of quantum typicality [22–25, 55–60], the trace in Eq. (12) can be replaced by a scalar product with a single pure state $|\varphi\rangle$ which is randomly drawn according to the unitary invariant Haar measure,

$$\mathcal{C}_{l,l'}(t) \approx \frac{\langle\varphi|\sqrt{\tilde{\varrho}_{l'}}\varrho_l(t)\sqrt{\tilde{\varrho}_{l'}}|\varphi\rangle}{\langle\varphi|\varphi\rangle} + \epsilon(|\varphi\rangle) \tag{13}$$

$$= \langle\psi(0)|\varrho_l(t)|\psi(0)\rangle = \langle\psi(t)|\varrho_l|\psi(t)\rangle , \tag{14}$$

where we have used the definition of $|\psi(0)\rangle$ from Eq. (3) and interpreted the time dependence as a property of the states and not of the operator. The combination of Eqs. (10) to (14) yields the typicality relation (4), where we have chosen $l' = L/2$ without loss of generality.

B. Construction of initial states

Concerning the construction of the pure state $|\psi(0)\rangle$ in Eq. (3), i.e., the evaluation of the square root $\sqrt{\tilde{\varrho}_{L/2}}$, the following comments are in order. On the one hand, in the case of $\varrho_l = S^z_{l,1} + S^z_{l,2}$ this procedure is rather simple since $S^z_{l,1} + S^z_{l,2}$ is naturally diagonal in the Ising basis, which is routinely used as our working basis. On the other hand, in the case of the local energy, $\varrho_l = h_l$ is not diagonal immediately. While this situation usually requires diagonalization, a complete diagonalization of h_l can still be avoided since h_l is a local operator acting nontrivially only on a small part of the Hilbert space. Thus, although the preparation of $|\psi(0)\rangle$ becomes more demanding in the case of $\varrho_l = h_l$, it certainly remains feasible and yields a powerful numerical approach as well. If one still wants to refrain from such square-root constructions, it is also possible to use *two* auxiliary pure states instead of just *one* (cf. Appendix A). It should be noted however, that the approach presented in this paper, using just a single pure state, will generally be more favorable concerning memory requirements and run time (even if the initial preparation of $|\psi(0)\rangle$ is more costly).

C. Pure-state propagation

Relying on the typicality relation (4), we calculate spatio-temporal correlation functions for spin and energy densities. The main advantage of this approach comes from the fact that the action of $e^{-i\mathcal{H}t}$ on the pure state $|\psi(0)\rangle$ can be efficiently evaluated *without* the diagonalization of $\mathcal{H}$, e.g., by means of a Trotter decomposition [80] (see also Appendix B), or also by other approaches [81–83]. Moreover, let us stress that the numerical costs of the Fourier transforms (5) and (6) are practically negligible. Therefore, we essentially obtain all information on the dynamics of either magnetization or energy from the time evolution of the *single* pure state $|\psi(t)\rangle$ and the measurement of L local operators ϱ_l, cf. Appendix C. In practice, this pure-state approach enables us to treat ladders with up to $L = 20$ rungs, i.e., 40 lattice sites in total. If not stated otherwise, we always take into account the full Hilbert space (e.g. $d \approx 10^{12}$ for $L = 20$).

D. Finite temperatures

Although the focus of this paper is on quantum dynamics at formally infinite temperature, let us briefly

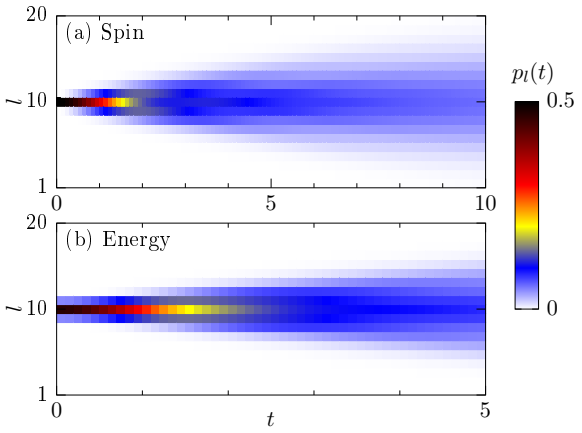

FIG. 2. (Color online) Real-time broadening of density profiles $p_l(t)$ for spin $\varrho_l = S^z_{l,1} + S^z_{l,2}$ and energy $\varrho_l = h_l$. The other parameters are $J_\parallel = J_\perp = 1$ and $L = 20$.

outline how finite-temperature correlations can be obtained based on pure-state calculations as well. On the one hand, a straightforward approach is the construction of the typical pure state $|\varphi_\beta\rangle$ according to [57, 60]

$$|\varphi_\beta\rangle = e^{-\beta\mathcal{H}/2}\,|\varphi\rangle \quad , \tag{15}$$

where the reference pure state $|\varphi\rangle$ corresponds to infinite temperature and has been introduced in Eq. (3). Analogous to the real-time evolution, the action of $e^{-\beta\mathcal{H}/2}$ can be efficiently evaluated by an iterative forward propagation, but now in imaginary time. More details on finite-temperature calculations using $|\varphi_\beta\rangle$ can be found in Appendix A.

On the other hand, another useful class of pure states $|\tilde{\varphi}_{\alpha,\beta}\rangle$, which has been put forward in Ref. [84], is constructed as

$$|\tilde{\varphi}_{\alpha,\beta}\rangle \propto e^{-\beta(\mathcal{H}-\alpha\varrho_{l'})/2}\,|\varphi\rangle \quad . \tag{16}$$

In particular, depending on the size of the control parameter α, these states can not only be used to obtain linear-response correlation functions, but also to calculate far-from-equilibrium quantum dynamics [21, 84].

Finally, let us note that, since the effective Hilbert-space dimension shrinks for $\beta > 0$, the statistical error ϵ of the typicality approximation, cf. Eq. (4), is generally larger compared to the infinite-temperature limit. Nevertheless, even for $\beta > 0$ this error still decreases exponentially with system size and accurate calculations remain possible for moderate temperatures.

V. RESULTS

We now present our numerical results. In Sec. V A, we start with the analysis of density dynamics in real space. The corresponding structure factors are then discussed for magnetization in Sec. V B and for energy in Sec. V C.

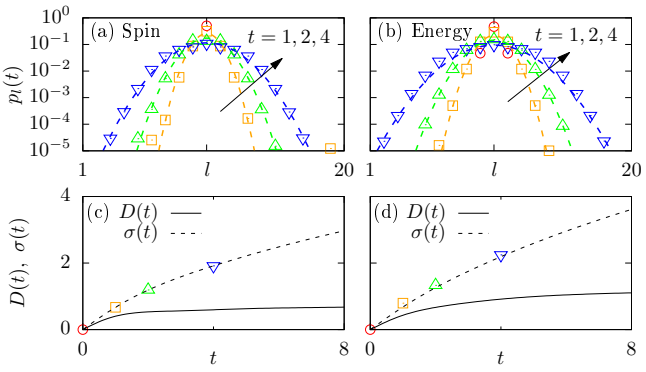

FIG. 3. (Color online) (a) and (b): Density profiles $p_l(t)$ for spin and energy, at fixed times $t = 0$ (δ peak) and $t = 1, 2, 4$ (arrow). The dashed lines are Gaussian fits to the data. (c) and (d): Widths of the density profiles (symbols) obtained from Eq. (8), as well as $D(t)$ and $\sigma(t)$ (lines) calculated from current autocorrelations, cf. Eqs. (7) and (9). For sufficiently long times, one finds $D(t) \approx$ const. The other parameters are $J_\parallel = J_\perp = 1$, $L = 20$ (densities), $L = 18$ (spin current), and $L = 15$ (energy current [67]).

A. Real-space dynamics

To begin with, let us focus on the isotropic case $J_\parallel = J_\perp = 1$. Starting with dynamics in time and real space, Figs. 2 (a) and (b) show the density profiles $p_l(t)$ of magnetization and energy for large systems with $L = 20$. One can clearly observe the initial δ peak at $t = 0$ (or almost δ peak [77]) which broadens for times $t > 0$. Moreover, on the (short) time scales depicted, $p_l(t)$ does not reach the boundaries of the system, i.e., trivial finite-size effects do not occur.

For a more detailed discussion, Figs. 3 (a) and (b) show cuts of $p_l(t)$ at fixed times $t = 0, 1, 2, 4$. For these times, one finds that the data are well described by Gaussians over several orders of magnitude,

$$p_l(t) \propto \exp\left[-\frac{(l - L/2)^2}{2\sigma(t)^2}\right] \quad . \tag{17}$$

While these Gaussians already suggest diffusion both for magnetization and energy (cf. Appendix D), it is only an sufficient criterion if $\sigma(t)$ scales as $\sigma(t) \propto \sqrt{t}$ as well. Consequently, Figs. 3 (c) and (d) show the widths of the density profiles obtained from Eq. (8) (symbols) in comparison with the respective quantities $D(t)$ and $\sigma(t)$ (lines), calculated from the current autocorrelations, cf. Eqs. (7) and (9). Generally, one observes an excellent agreement between density and current dynamics. Moreover, after a linear increase at short times, $D(t)$ eventually saturates at a constant plateau $D(t) \approx$ const., and correspondingly $\sigma(t) \propto \sqrt{t}$. Thus, based on our numerical analysis in time and real space, we unveil the existence of diffusive transport in the spin-1/2 ladder both for magnetization as well as energy. This is a first main result of this paper.

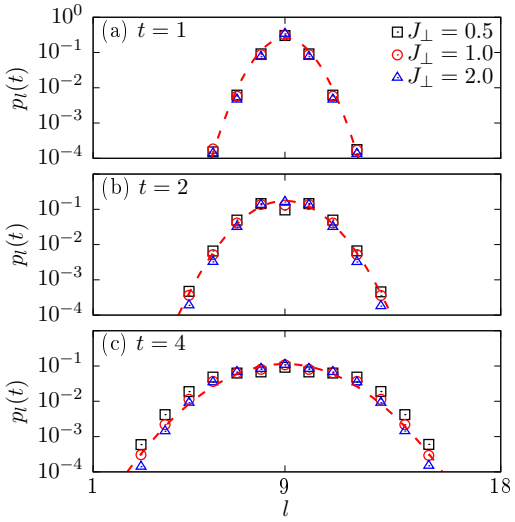

FIG. 4. (Color online) Magnetization profiles $p_l(t)$ at fixed times $t = 1, 2, 4$. Comparison between different interchain couplings $J_\perp = 0.5, 1, 2$. The dashed lines are Gaussian fits to the data. The other parameters are $J_\parallel = 1$ and $L = 18$.

Let us now briefly present magnetization profiles also for other ratios $J_\perp/J_\parallel \neq 1$. To this end, Fig. 4 shows the real-space density profiles $p_l(t)$ at fixed times $t = 1, 2, 4$ for interchain couplings $J_\perp = 0.5, 1, 2$ ($J_\parallel = 1$). Generally, we find that the profiles are very similar to each other for all t and $J_\perp$ shown here. In particular, all profiles are convincingly described by Gaussian fits over several orders of magnitude.

B. Spin structure factor

Next, let us also study magnetization dynamics in momentum space, where the lattice diffusion equation decouples into separate Fourier modes (cf. Appendix D).

1. *Long-wavelength limit*

In Fig. 5 (a), the density modes $p_q(t)$ for $J_\parallel = J_\perp = 1$ are shown for various momenta q in a semilogarithmic plot. On the one hand, for large $q = \pi$, $p_q(t)$ exhibits pronounced oscillations and essentially decays on a time scale $t \sim 5$. On the other hand, for the two smallest wave numbers $k = 1$ and $k = 2$, we find clean exponential relaxation

$$p_q(t) \propto e^{-\tilde{q}^2 D t} \ , \tag{18}$$

where we have introduced the abbreviation $\tilde{q}^2 = 2[1 - \cos(q)] \approx q^2$ for sufficiently small q, and $D = \text{const.}$ can be extracted from the constant plateau in Fig. 3 (c). Going from time to frequency domain, Fig. 5 (b) shows the corresponding dynamical structure factors $p_q(\omega)$ for

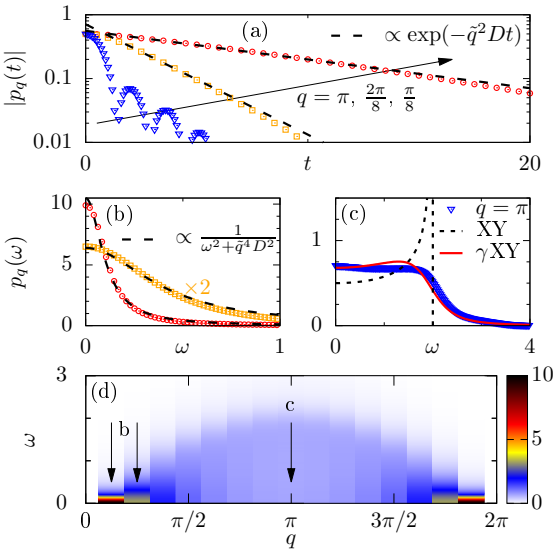

FIG. 5. (Color online) Spin dynamics. (a): $p_q(t)$ for wave numbers $k = 1, 2, 8$ in a semilogarithmic plot. Lines are exponential functions according to Eq. (18). (b): $p_q(\omega)$ for $k = 1, 2$. Lines are Lorentzians according to Eq. (19). (c): $p_q(\omega)$ for $k = 8$. Comparison with XY model [Eq. (20)] and an effective model (γXY) where the original memory kernel of the Bessel function is exponentially damped (here $\gamma = 0.6$) [85]. The XY data is multiplied by a factor of 2 in order to account for the two legs of the ladder. (d): $p_q(\omega)$ in the full Brillouin zone. Arrows show the data of panels (b) and (c). Other parameters: $J_\parallel = J_\perp = 1$, $L = 16$, and $\delta\omega = \pi/150$.

$k = 1, 2$. One observes that the data can be accurately described by Lorentzians of the form,

$$p_q(\omega) \propto \frac{1}{\omega^2 + \tilde{q}^4 D^2} \ . \tag{19}$$

Note that, while we display the time data in Fig. 5 (a) only up to intermediate time scales, the Fourier transform (6) is routinely performed for a much longer cut-off time (here $t_{\max} = 150$) in order to achieve a high frequency resolution. The exponential relaxation [Fig. 5 (a)] and the Lorentzian line shapes [Fig. 5 (b)] clearly confirm our earlier observations in the context of Fig. 3, i.e., the occurrence of genuine spin diffusion in the spin-1/2 ladder. This is another main result of the present work.

Eventually, Fig. 5 (d) shows the dynamical structure factor $p_q(\omega)$ for all momenta q. Let us stress again that within our numerical approach the calculation of these density modes essentially does not require any additional resources. On the one hand, for small momenta $q \to 0$, one can clearly identify the diffusion peaks discussed above. On the other hand, in the center of the Brillouin zone, we find that $p_q(\omega)$ exhibits a broad continuum. This short-wavelength limit will be discussed below in more detail.

In order to corroborate once more that the emergence of diffusive transport is not restricted to the isotropic

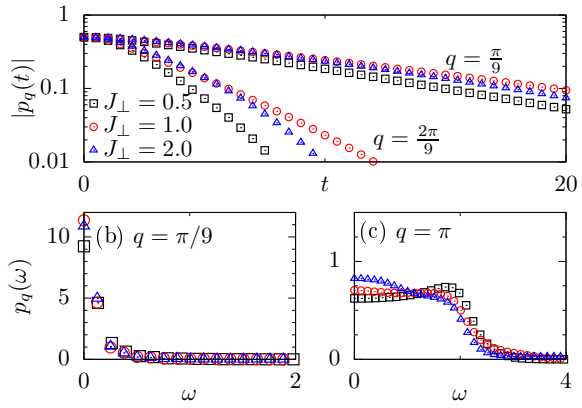

FIG. 6. (Color online) Spin dynamics for different interchain couplings $J_\perp = 0.5, 1, 2$. (a): $p_q(t)$ for the two smallest wave numbers $k = 1, 2$. (b) and (c): $p_q(\omega)$ for $k = 1$ and $k = 9$, respectively. Other parameters: $J_\parallel = 1$, $L = 18$, and $\delta\omega = \pi/25$.

point, Fig. 6 shows the structure factors $p_q(t)$ and $p_q(\omega)$ for $J_\perp = 0.5, 1, 2$. For the smallest wave number $k = 1$, we find a clean exponential decay of $p_q(t)$ with a decay rate $-\tilde{q}^2 D$, which is almost identical for all $J_\perp$ shown here. This fact is also reflected in the Lorentzian shape of $p_q(t)$ for this momentum [Fig. 6 (b)], which essentially coincides for all strengths of interchain couplings. On the other hand, for wave number $k = 2$, we find that $p_q(t)$ for $J_\perp = 0.5$ shows some deviations from an exponential, i.e., the hydrodynamic regime becomes smaller for smaller $J_\perp$, which can be explained by the increased mean free path of spin excitations.

2. *Short-wavelength limit*

In addition to the long-wavelength limit, Fig. 5 (c) shows $p_q(\omega)$ at momentum $q = \pi$. For this momentum, one finds that $p_q(\omega)$ is practically ω-independent up to $\omega \lesssim 2$ and exhibits a constant plateau. It is instructive to compare this result to the dynamics of the one-dimensional XY model. Since the XY chain is equivalent to a model of free fermions, $p_q(\omega)$ is known exactly [74] and reads (for $\beta \to 0$, $J_\parallel = 1$, and $q = \pi$)

$$p_{q=\pi}(\omega) = \int_{-\infty}^{\infty} e^{i\omega t} \frac{\mathcal{J}_0(2t)}{4}\, \mathrm{d}t = \frac{\Theta(2 - |\omega|)}{2\sqrt{4 - \omega^2}} \,. \tag{20}$$

Here, $\mathcal{J}_0(t)$ is the Bessel function of first kind (and order zero), and $p_{q=\pi}(\omega)$ exhibits a square-root divergence at $\omega = 2$, cf. Fig. 5 (c). Following an approach introduced in Ref. [85], the dynamics $p_q(t) \propto \mathcal{J}_0(2t)$ is interpreted as being generated by an integro-differential equation comprising a *memory kernel* $K(t)$,

$$\frac{\mathrm{d}}{\mathrm{d}t}\, p_q(t) = -\int_0^t K(t - t') p_q(t') \mathrm{d}t' \,. \tag{21}$$

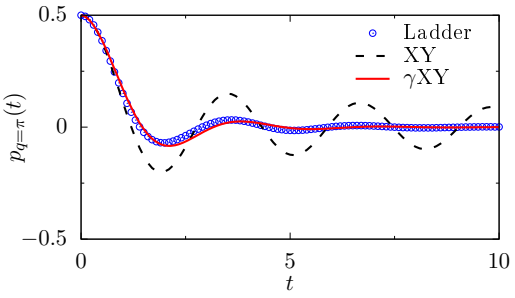

FIG. 7. (Color online) Comparison of $p_{q=\pi}(t)$ between the spin ladder with $J_\parallel = J_\perp = 1$ [Fig. 5 (a) from main text], the bare XY model (Bessel function), and the effective dynamics $\tilde{p}_q(t)$ (γXY) [see Eqs. (21) and (23)] with damping $\gamma = 0.6$. The XY data is multiplied by a factor of 2 in order to account for the two legs of the ladder.

Equation (21) establishes a direct correspondence between $p_q(t)$ and $K(\tau)$ and can be evaluated in both directions. Thus, given the original dynamics $p_q(t) \propto \mathcal{J}_0(2t)$, the respective memory kernel $K(\tau)$ can be calculated, e.g., numerically. In fact, given the expression in Eq. (20), $K(\tau)$ can be even obtained analytically and reads,

$$K(\tau) = \frac{2\mathcal{J}_1(2\tau)}{\tau} \,. \tag{22}$$

Comparing the bare XY model with the full spin ladder (1), the additional rung couplings as well as the $S^z_{\mathbf{r}} S^z_{\mathbf{r}'}$ terms are treated as a perturbation giving rise to an exponential damping of this memory kernel (for small perturbations) [85, 86],

$$\tilde{K}(\tau) = K(\tau) e^{-\gamma\tau} \,. \tag{23}$$

This new memory kernel $\tilde{K}(\tau)$ is then used to numerically evaluate Eq. (21) in order to obtain the new (damped) dynamics $\tilde{p}_q(t)$. As shown in Fig. 5 (c), the effective dynamics generated by this (heuristic) approach with $\gamma = 0.6$ reproduces the structure factor of the spin ladder remarkably well, even though the perturbation is not small. Moreover, as shown in Fig. 7, this convincing agreement between spin ladder and effective model can not only be observed in frequency space, but also in real time. Eventually, let us note that, while $\gamma = 0.6$ is found to describe the data most accurately, a more quantitative understanding of this specific value goes beyond the scope of the present paper, see also Ref. [86].

Thus, while clear signatures of diffusion can be found for long-wavelength modes [cf. Figs. 5 (a) and (b)], the relaxation of $p_q(t)$ for $q \to \pi$ can be qualitatively understood as the (damped) dynamics of free fermions, e.g., since the wavelength is smaller than the mean-free path. Note that similar behavior has been found also for XXZ chains [74, 87].

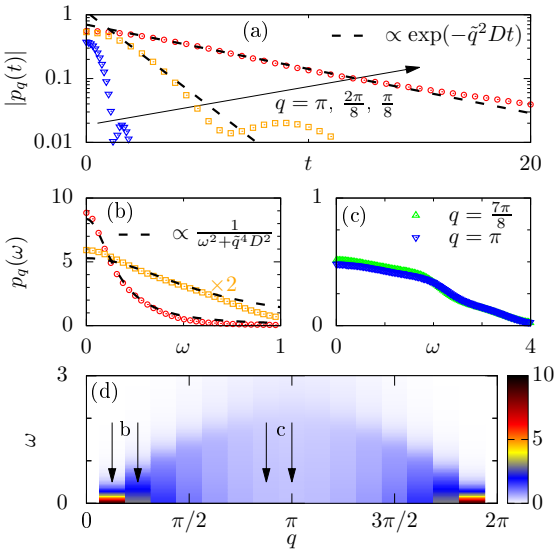

FIG. 8. (Color online) Energy dynamics. (a): $p_q(t)$ for $k = 1, 2, 8$. (b) $p_q(\omega)$ for $k = 1, 2$. (c): $p_q(\omega)$ for $k = 7, 8$. (d): $p_q(\omega)$ in the full Brillouin zone. Other parameters: $J_\parallel = J_\perp = 1$, $L = 16$, and $\delta\omega = \pi/150$

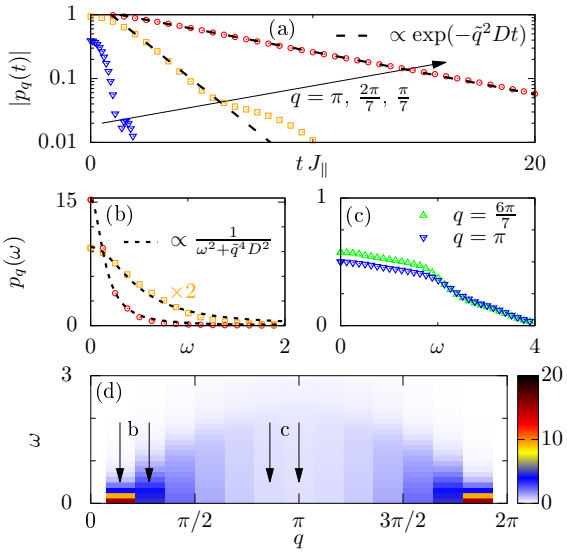

FIG. 9. (Color online) Energy dynamics in the presence of a magnetic field. Calculations are performed in the subsector with $S^z = 0$ only. The other parameters are: $J_\parallel = J_\perp = B = 1$, $L = 14$, and $\delta\omega = \pi/25$.

C. Energy structure factor

We now also present results for energy dynamics in momentum space. Analogously to the discussion in the context of Fig. 5, Fig. 8 shows the energy structure factors $p_q(t)$ and $p_q(\omega)$ of the isotropic spin ladder for short and long wavelengths. Generally, the results for energy dynamics are very similar to the previously discussed case of magnetization, i.e., $p_q(t)$ decays exponentially for small q while the corresponding $p_q(\omega)$ exhibits a Lorentzian line shape. Thus, the data shown in Fig. 8 confirm the existence of diffusive energy transport as well, see also Refs. [62, 66, 67].

Finally, it is instructive to discuss the effect of an additional uniform magnetic field $B > 0$ in the z direction, i.e., the new local energy $\tilde{h}_l$ reads

$$\tilde{h}_l = h_l + \frac{B}{2} \sum_{n=l}^{l+1} \sum_{k=1}^{2} S^z_{n,k} \ , \tag{24}$$

where h_l is defined according to Eq. (1). Such a modification results in a magnetothermal correction and the heat current takes on the form

$$\tilde{j}_E = j_E + B j_S \ , \tag{25}$$

where the spin current j_S is independent of B. For specific expressions of j_S and j_E, see Appendix A. In Fig. 9, we depict the energy structure factors $p_q(t)$ and $p_q(\omega)$ in time as well as frequency domain for various momenta q. Note that we restrict ourselves to the symmetry subspace with magnetization $S^z = 0$. Generally, we find that the presence of a finite magnetic field does not qualitatively change the behavior of $p_q(t)$ and $p_q(\omega)$. Again, one can observe an exponential decay for the two smallest wave numbers $k = 1, 2$ and correspondingly a Lorentzian line shape in frequency space at these momenta. Compared to the results with $B = 0$ shown in Fig. 8, one might even argue that those signatures of diffusion are slightly improved due to the finite magnetic field.

VI. CONCLUSION

To summarize, we have studied spin and energy dynamics in the spin-1/2 ladder for large systems with up to 40 lattice sites. Our state-of-the-art numerical simulations have unveiled the existence of genuine diffusion both for spin and energy. In particular, this finding is based on four distinct signatures which have all been equally well detected: (i) Gaussian density profiles, (ii) time-independent diffusion coefficients, (iii) exponentially decaying density modes, and (iv) Lorentzian line shapes of the dynamical structure factor. Combining (i) - (iv), this paper provides a comprehensive picture of high-temperature dynamics in the spin-1/2 ladder. Promising directions of research include, e.g., the application of the pure-state approach to a larger class of condensed matter systems and a wider range of temperatures [88]. In this context, it is also an intriguing question if the observed signatures of diffusion persist at lower temperatures.

Acknowledgments

This work has been funded by the Deutsche Forschungsgemeinschaft (DFG) - GE 1657/3-1; STE 2243/3-1 - within the DFG Research Unit FOR 2692 - 355031190. Additionally, we gratefully acknowledge the computing time, granted by the "JARA-HPC Vergabegremium" and provided on the "JARA-HPC Partition" part of the supercomputer "JUWELS" at Forschungszentrum Jülich. J.H. has been supported by the US Department of Energy (DOE), Office of Science, Basic Energy Sciences (BES), Materials Sciences and Engineering Division.

Appendix A: Current operators and autocorrelations

The spin current j_S is defined as [66]

$$j_S = J_\parallel \sum_{l=1}^{L} \sum_{k=1}^{2} \left(S^x_{l,k} S^y_{l+1,k} - S^y_{l,k} S^x_{l+1,k} \right) \ . \tag{A1}$$

Moreover, the energy current $j_E = j_\parallel + j_\perp$ can be written as a sum of a longitudinal and a perpendicular part which read [62, 67]

$$j_\parallel = J_\parallel^2 \sum_{l=1}^{L} \sum_{k=1}^{2} \mathbf{S}_{l-1,k} \cdot (\mathbf{S}_{l,k} \times \mathbf{S}_{l+1,k}) \ , \tag{A2}$$

$$j_\perp = \frac{J_\parallel J_\perp}{2} \sum_{l=1}^{L} \sum_{k=1}^{2} (\mathbf{S}_{l-1,k} - \mathbf{S}_{l+1,k}) \cdot (\mathbf{S}_{l,k} \times \mathbf{S}_{l,3-k}) \ . \tag{A3}$$

In order to calculate current-current correlation functions $\langle j(t) j \rangle$ by means of a typicality-based approach directly (at finite or infinite temperature), we use the two auxiliary pure states [60]

$$|\varphi(\beta, t)\rangle = e^{-i\mathcal{H}t} e^{-\beta\mathcal{H}/2} |\varphi\rangle \ , \tag{A4}$$

$$|\phi(\beta, t)\rangle = e^{-i\mathcal{H}t} j e^{-\beta\mathcal{H}/2} |\varphi\rangle \ , \tag{A5}$$

which only differ by the additional current operator in Eq. (A5), and where $|\varphi\rangle$ is again a random state drawn according to the Haar measure, cf. Eq. (3). Then, we can write [60]

$$\langle j(t) j \rangle = \frac{\langle \varphi(\beta, t) | \, j \, | \phi(\beta, t) \rangle}{\langle \varphi(\beta, 0) | \varphi(\beta, 0) \rangle} + \epsilon(|\varphi\rangle) \ , \tag{A6}$$

where again $\epsilon(|\varphi\rangle) \propto 1/\sqrt{d}$ for $\beta \to 0$. Of course, by replacing the current operator j in Eqs. (A5) and (A6), it is straightforward to generalize the above approach in order to calculate dynamic correlation functions also for other operators.

While we already introduced the time-dependent diffusion coefficient $D(t)$ for spin and energy transport in Eq. (7), the respective ac-conductivities at finite frequency ω are given by the Fourier transform of the current autocorrelations,

$$\mathrm{Re}\ \sigma(\omega) = \frac{1 - e^{-\beta\omega}}{\omega L} \, \mathrm{Re} \int_0^\infty e^{i\omega t} \, \langle j_S(t) j_S \rangle \, \mathrm{d}t \ , \tag{A7}$$

$$\mathrm{Re}\ \kappa(\omega) = \beta \frac{1 - e^{-\beta\omega}}{\omega L} \, \mathrm{Re} \int_0^\infty e^{i\omega t} \, \langle j_E(t) j_E \rangle \, \mathrm{d}t \ . \tag{A8}$$

Note that the spin conductivity $\sigma(\omega)$ from Eq. (A7) must not be confused with the spatial variance $\sigma(t)$ introduced in Eq. (8). Omitting the possibility of finite Drude weights, the corresponding dc-conductivities are given by $\lim_{\omega \to 0} \sigma[\kappa](\omega) = \sigma[\kappa]_{\mathrm{dc}}$ and can be connected to the diffusion constant via an Einstein relation $D = D(t \to \infty) = \sigma[\kappa]_{\mathrm{dc}}/\chi$, cf. Eq. (7). Let us note that, since the Fourier transforms in Eqs. (A7) and (A8) can in practice be only evaluated up to a finite cutoff time $t_{\mathrm{max}} < \infty$, the frequency resolution of $\sigma[\kappa](\omega)$ is finite as well [see also Eq. (6) in the main text].

In Figs. 10 (a) and (b), the current autocorrelations $\langle j(t) j \rangle$ at $\beta = 0$ are shown for spin and energy transport, respectively. While in Fig. 10 (a) we show data

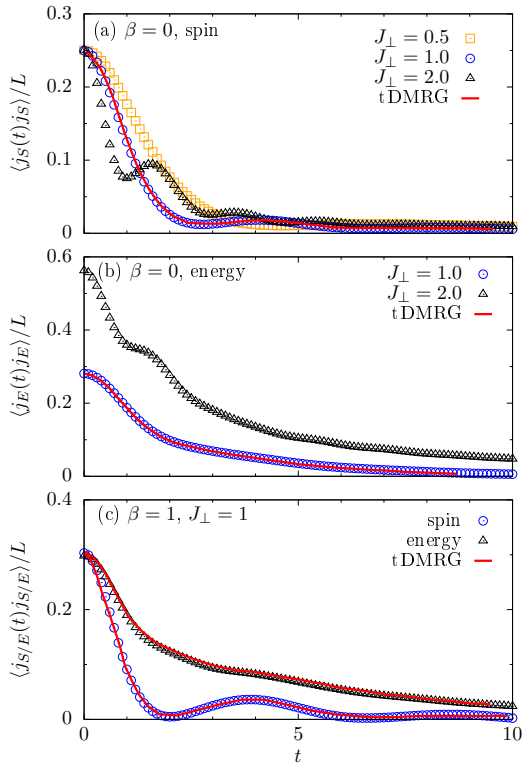

FIG. 10. (Color online) Current autocorrelations. (a): Spin current j_S for $J_\perp = 0.5, 1, 2$ and $\beta = 0$. (b): Energy current j_E for $J_\perp = 1, 2$ and $\beta = 0$. (c): Spin and energy current for $\beta = 1$ and $J_\perp = 1$. For comparison, we depict tDMRG data digitized from Ref. [66]. Note that in the case of j_E we restrict ourselves to the symmetry subspaces with momentum $k = 0$. Other parameters: $J_\parallel = 1$, $L = 13$ (spin), $L = 15$ (energy).

for smaller systems with $L = 13$ rungs only, the energy current in Fig. 10 (b) is calculated for systems with $L = 15$. Note however that in the latter case, we restrict ourselves to the symmetry subspaces with momentum $k = 0$ as the current is known to be essentially independent of k for such system sizes. [This *crystal momentum* k should not be confused with the wave number k below Eq. (5)]. In all cases shown here, we observe that $\langle j(t)j\rangle$ decays to approximately zero, consistent with the absence of ballistic transport in a nonintegrable system. In the case $J_\perp/J_\parallel = 1$, our results are additionally compared to data digitized from Ref. [66] obtained by a time-dependent density matrix renormalization group (tDMRG) approach. Generally, one finds a convincing agreement between both methods, i.e., our data for $L = 13, 15$ is free of significant finite-size effects and represents the thermodynamic limit. In Fig. 10 (c), spin and energy autocorrelations are depicted for the finite temperature $\beta = 1$. Also in this case, we observe that the pure-state method accurately reproduces the tDMRG data. Thus, typical pure states yield an efficient approach to correlation functions at finite temperatures as well.

In Figs. 11 (a) and (b) the respective ac-conductivities $\sigma(\omega)$ and $\kappa(\omega)$ at $\beta = 0$ are shown, i.e., the Fourier transforms of the data in Figs. 10 (a) and (b). Particularly, we compare data with two different frequency resolutions $\delta\omega = \pi/10$ and $\delta\omega = \pi/50$, i.e., a rather short and significantly longer cutoff time $t_{\max}$ in Eqs. (A7) and (A8). In all cases, we observe a well-behaved dc-conductivity $\sigma[\kappa]_{\rm dc} > 0$ which does not (significantly) depend on $t_{\max}$, except $\kappa(\omega)$ for $J_\perp = 2$. Moreover, our data is again in good agreement with existing data obtained by tDMRG [66] and by the microcanonical Lanczos method [62].

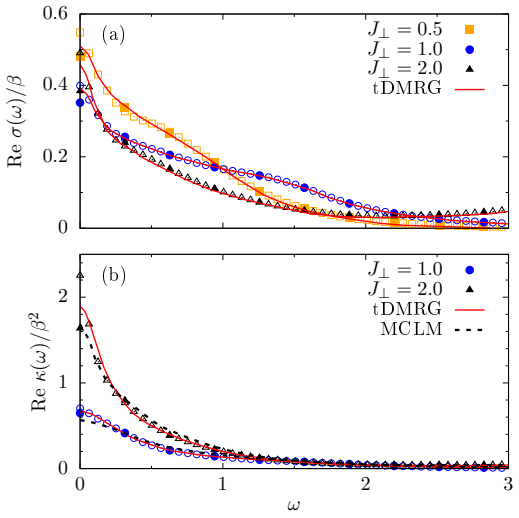

FIG. 11. (Color online) (a): Spin conductivity $\sigma(\omega)$ for $J_\perp = 0.5, 1, 2$. (b): Energy conductivity $\kappa(\omega)$ for $J_\perp = 1, 2$. We show data for two different frequency resolutions, $\delta\omega = \pi/10$ (filled symbols), $\delta\omega = \pi/50$ (open symbols). For comparison, tDMRG data digitized from Ref. [66] is shown. In (b), we also compare to data obtained from the microcanonical Lanzcos method (MCLM) [62]. In the case of $\kappa(\omega)$ we restrict ourselves to the symmetry subspaces with momentum $k = 0$. Other parameters: $J_\parallel = 1$, $\beta = 0$, $L = 13$ (spin), and $L = 15$ (energy).

Appendix B: Trotter decomposition

Let us briefly give some details on the time evolution of pure quantum states by means of a Trotter decomposition. To begin with, we note that the time-dependent Schrödinger equation

$$i\partial_t \,|\psi(t)\rangle = \mathcal{H}\,|\psi(t)\rangle \tag{B1}$$

is formally solved by

$$|\psi(t')\rangle = U(t,t')\,|\psi(t)\rangle \ , \tag{B2}$$

with $U(t,t') = e^{-i\mathcal{H}(t'-t)}$, where we have set $\hbar = 1$. While the exact evaluation of Eq. (B2) requires the diagonalization of $\mathcal{H}$, we here approximate the time-evolution operator $U(t,t')$ by means of a Trotter product formula. Specifically, a second-order approximation of $U(t,t+\delta t) = U(\delta t)$ is given by

$$\widetilde{U}_2(\delta t) = e^{-i\frac{\delta t}{2}\mathcal{H}_k}\cdots e^{-i\frac{\delta t}{2}\mathcal{H}_1} e^{-i\frac{\delta t}{2}\mathcal{H}_1}\cdots e^{-i\frac{\delta t}{2}\mathcal{H}_k} \ , \tag{B3}$$

where $\mathcal{H} = \mathcal{H}_1 + \cdots + \mathcal{H}_k$. This approximation is then bounded by

$$||U(\delta t) - \widetilde{U}_2(\delta t)|| \ll c_2\,\delta t^3 \ , \tag{B4}$$

where c_2 is a positive constant. In practice, the Hamiltonian is decomposed into the x, y, and z components of the spin operators, i.e., $\mathcal{H} = \mathcal{H}_x + \mathcal{H}_y + \mathcal{H}_z$. Since the computational basis states are eigenstates of the S^z operators, the representation $e^{-i\delta t\mathcal{H}_z}$ is diagonal by construction and only changes the input state by altering the phase of each of the basis vectors. Using an efficient basis rotation into the eigenstates of the S^x or S^y operators, the operators $e^{-i\delta t\mathcal{H}_x}$ and $e^{-i\delta t\mathcal{H}_y}$ can act as $e^{-i\delta t\mathcal{H}_z}$ as well [80].

Appendix C: Fourier transforms

Let us comment on the derivation of Eqs. (5) and (6) from the main part of this paper. Referring to Eq. (4), we realize that a cut through the density profile $p_l(t)$ at fixed lattice site l is equivalent to the correlation function $\langle\varrho_l(t)\varrho_{L/2}\rangle$. It is now instructive to perform the following

calculation

$$\langle \varrho_q(t)\varrho_{-q}\rangle = \frac{1}{L}\sum_{l=1}^{L}\sum_{l'=1}^{L} e^{iq(l-l')}\langle \varrho_l(t)\varrho_{l'}\rangle \tag{C1}$$

$$= \sum_{l=1}^{L} e^{iql}\langle \varrho_{L/2+l}(t)\varrho_{L/2}\rangle \tag{C2}$$

$$= \sum_{l=1}^{L} e^{iq(l-L/2)} p_l(t) = p_q(t) \ , \tag{C3}$$

where we have exploited translational invariance in order to compress the original double sum. Thus, we find that the intermediate structure factor $\langle \varrho_q(t)\varrho_{-q}\rangle$ can be easily obtained by a lattice Fourier transform of the real-space correlations. Furthermore, this momentum-space correlation function can also be transferred to what is usually referred to as the *dynamical structure factor* $S(q,\omega)$ by another Fourier transform from time to frequency domain,

$$S(q,\omega) = \int_{-\infty}^{\infty} e^{i\omega t}\langle \varrho_q(t)\varrho_{-q}\rangle \ \mathrm{d}t \tag{C4}$$

$$\approx \int_{-t_{\max}}^{t_{\max}} e^{i\omega t} p_q(t) \ \mathrm{d}t = p_q(\omega) \ , \tag{C5}$$

where the finite cutoff time $t_{\max}$ yields a frequency resolution $\delta\omega = \pi/t_{\max}$. Thus, starting from the correlations $p_l(t)$ it is straightforward to also obtain correlation functions in momentum and frequency domain, which makes our pure-state method a rather powerful numerical approach.

Appendix D: Diffusion in lattice models

In this section, let us discuss in more detail how to detect diffusion in lattice models. To begin with, a process is called diffusive if it fulfills the lattice diffusion equation

$$\frac{\mathrm{d}}{\mathrm{d}t}\, p_l(t) = D\left[p_{l-1}(t) - 2p_l(t) + p_{l+1}(t)\right] \ , \tag{D1}$$

with the *time-independent* diffusion constant D. In the case of an initial δ peak profile at $l = L/2$, a specific solution for the time dependence of $p_t(t)$ is given by [54]

$$p_l(t) - p_{\mathrm{eq}} = \frac{1}{2}\exp(-2Dt)\,\mathcal{B}_{l-L/2}(2Dt) \ , \tag{D2}$$

where $\mathcal{B}_l(t)$ is the modified Bessel function of the first kind and $p_{\mathrm{eq}} = p_{l\neq L/2}(0)$ denotes the homogeneous background. (Note that in this paper we have $p_{\mathrm{eq}} = 0$ since $\mathrm{Tr}[\varrho_l] = 0$.) In case of sufficiently large L and long t, i.e., if the discrete lattice momenta q become dense, this lattice solution can be well approximated by a Gaussian. Such Gaussians have been observed in Figs. 3 (a) and (b). Specifically, the spatial variance of these Gaussians is then also given by $\sigma^2(t) = 2Dt$, i.e., $\sigma(t) \propto \sqrt{t}$.

Given some general density distribution, it is in some cases instructive to study the dynamics in momentum space as well. In this context, a Fourier transform of Eq. (D1) yields

$$\frac{\mathrm{d}}{\mathrm{d}t}\, p_q(t) = -2D(1-\cos q)p_q(t) \ . \tag{D3}$$

Apparently the L different Fourier modes $p_q(t)$ are completely decoupled and their exponentially decaying solutions have been already given in Eq. (18).

[1] D. C. Johnston, R. K. Kremer, M. Troyer, X. Wang, A. Klümper, S. L. Bud'ko, A. F. Panchula, and P. C. Canfield, Phys. Rev. B **61**, 9558 (2000).
[2] A. V. Sologubenko, K. Giannó, H. R. Ott, U. Ammerahl, and A. Revcolevschi, Phys. Rev. Lett. **84**, 2714 (2000).
[3] C. Hess, C. Baumann, U. Ammerahl, B. Büchner, F. Heidrich-Meisner, W. Brenig, and A. Revcolevschi, Phys. Rev. B **64**, 184305 (2001).
[4] B. Lake, D. A. Tennant, J.-S. Caux, T. Barthel, U. Schollwöck, S. E. Nagler, and C. D. Frost, Phys. Rev. Lett. **111**, 137205 (2013).
[5] M. Mourigal, M. Enderle, A. Klöpperpieper, J.-S. Caux, A. Stunault, and H. M. Rønnow, Nat. Phys. **9**, 435 (2013).
[6] K. R. Thurber, A. W. Hunt, T. Imai, and F. C. Chou, Phys. Rev. Lett. **87**, 247202 (2001).
[7] H. Maeter, A. A. Zvyagin, H. Luetkens, G. Pascua, Z. Shermadini, R. Saint-Martin, A. Revcolevschi, C. Hess, and H.-H. Klauss, J. Phys.: Condens. Matter **25**, 365601 (2013).
[8] S. A. Wolf, D. D. Awschalom, R. A. Buhrman, J. M. Daughton, S. von Molnár, M. L. Roukes, A. Y. Chtchelkanova, and D. Treger, Science **294**, 1488 (2001).
[9] M. A. Cazalilla and M. Rigol, New J. Phys. **12**, 055006 (2010).
[10] Y. Ikhlef, J. L. Jacobsen, and H. Saleur, Phys. Rev. Lett. **108**, 081601 (2012).
[11] A. Polkovnikov, K. Sengupta, A. Silva, and M. Vengalattore, Rev. Mod. Phys. **83**, 863 (2011).
[12] J. Eisert, M. Friesdorf, and C. Gogolin, Nat. Phys. **11**, 124 (2015).
[13] C. Gogolin and J. Eisert, Rep. Prog. Phys. **79**, 056001 (2016).
[14] L. D'Alessio, Y. Kafri, A. Polkovnikov, and M. Rigol, Adv. Phys. **65**, 239 (2016).
[15] T. Langen, R. Geiger, and J. Schmiedmayer, Ann. Rev. Condens. Matter Phys. **6**, 201 (2015).
[16] S. Trotzky, Y-A. Chen, A. Flesch, I. P. McCulloch, U. Scholwöck, J. Eisert, and I. Bloch, Nat. Phys. **8**, 325 (2012).
[17] R. Blatt and C. F. Roos, Nat. Phys. **8**, 277 (2012).
[18] J. M. Deutsch, Phys. Rev. A **43**, 2046 (1991).

[19] M. Srednicki, Phys. Rev. E **50**, 888 (1994).
[20] M. Rigol, V. Dunjko, and M. Olshanii, Nature **452**, 854 (2008).
[21] J. Richter, J. Gemmer, and R. Steinigeweg, arXiv:1805.11625.
[22] J. Gemmer, M. Michel, and G. Mahler, *Quantum Thermodynamics* (Springer, Berlin, 2004).
[23] S. Popescu, A. J. Short, and A. Winter, Nat. Phys. **2**, 754 (2006).
[24] S. Goldstein, J. L. Lebowitz, R. Tumulka, and N. Zanghì, Phys. Rev. Lett. **96**, 050403 (2006).
[25] P. Reimann, Phys. Rev. Lett. **99**, 160404 (2007).
[26] U. Schollwöck, Rev. Mod. Phys. **77**, 259 (2005); Ann. Phys. **326**, 96 (2011).
[27] X. Zotos, F. Naef, and P. Prelovšek, Phys. Rev. B **55**, 11029 (1997).
[28] T. Prosen and E. Ilievski, Phys. Rev. Lett. **111**, 057203 (2013).
[29] L. Vidmar and M. Rigol, J. Stat. Mech. **2016**, 064007 (2016).
[30] F. Heidrich-Meisner, A. Honecker, D. C. Cabra, and W. Brenig, Phys. Rev. B **68**, 134436 (2003); F. Heidrich-Meisner, A. Honecker, and W. Brenig, Eur. Phys. J. Special Topics **151**, 135 (2007).
[31] J. Sirker, R. G. Pereira, and I. Affleck, Phys. Rev. B **83**, 035115 (2011).
[32] M. Žnidarič, Phys. Rev. Lett. **106**, 220601 (2011).
[33] R. Steinigeweg and W. Brenig, Phys. Rev. Lett. **107**, 250602 (2011).
[34] C. Karrasch, J. E. Moore, and F. Heidrich-Meisner, Phys. Rev. B **89**, 075139 (2014).
[35] R. Steinigeweg, F. Jin, D. Schmidtke, H. de Raedt, K. Michielsen, and J. Gemmer, Phys. Rev. B **95**, 035155 (2017).
[36] M. Ljubotina, M. Žnidarič, and T. Prosen, Nat. Comm. **8**, 16117 (2017).
[37] T. Prosen and M. Žnidarič, Phys. Rev. B **86**, 125118 (2012).
[38] C. Karrasch, T. Prosen, and F. Heidrich-Meisner, Phys. Rev. B **95**, 060406(R) (2017).
[39] R. Steinigeweg, F. Jin, H. De Raedt, K. Michielsen, and J. Gemmer, Phys. Rev. E **96**, 020105(R) (2017).
[40] O. A. Castro-Alvaredo, B. Doyon, and T. Yoshimura, Phys. Rev. X **6**, 041065 (2016).
[41] B. Bertini, M. Collura, J. De Nardis, and M. Fagotti, Phys. Rev. Lett. **117**, 207201 (2016).
[42] J. De Nardis, D. Bernard, and B. Doyon, Phys. Rev. Lett. **121**, 160603 (2018).
[43] A. L. Chernyshev and A. V. Rozhkov, Phys. Rev. Lett. **116**, 017204 (2016).
[44] K. R. Hazzard, M. van den Worm, M. Foss-Feig, S. R. Manmana, E. G. Dalla Torre, T. Pfau, M. Kastner, and A. M. Rey, Phys. Rev. A **90**, 063622 (2014).
[45] C. Karrasch, R. Ilan, and J. E. Moore, Phys. Rev. B **88**, 195129 (2013).
[46] A. Metavitsiadis, X. Zotos, O. S. Barišić, and P. Prelovšek, Phys. Rev. B **81**, 205101 (2010).
[47] J. Herbrych, J. Kokalj, and P. Prelovšek, Phys. Rev. Lett. **111**, 147203 (2013).
[48] C. W. von Keyserlingk, T. Rakovszky, F. Pollmann, and S. L. Sondhi, Phys. Rev. X **8**, 021013 (2018).
[49] A. Nahum, S. Vijay, and J. Haah, Phys. Rev. X **8**, 021014 (2018).
[50] V. Khemani, A. Vishwanath, and D. A. Huse, Phys. Rev. X **8**, 031057 (2018).
[51] M. Michel, G. Mahler, and J. Gemmer, Phys. Rev. Lett. **95**, 180602 (2005).
[52] C. Mejía-Monasterio, T. Prosen, and G. Casati, Europhys. Lett. **72**, 520 (2005).
[53] M. Medenjak, K. Klobas, and T. Prosen, Phys. Rev. Lett. **119**, 110603 (2017).
[54] J. Richter, F. Jin, H. De Raedt, K. Michielsen, J. Gemmer, and R. Steinigeweg, Phys. Rev. B **97**, 174430 (2018).
[55] A. Hams and H. De Raedt, Phys. Rev. E **62**, 4365 (2000).
[56] T. Iitaka and T. Ebisuzaki, Phys. Rev. Lett. **90**, 047203 (2003).
[57] S. Sugiura and A. Shimizu, Phys. Rev. Lett. **111**, 010401 (2013).
[58] T. A. Elsayed and B. V. Fine, Phys. Rev. Lett. **110**, 070404 (2013).
[59] T. Monnai and A. Sugita, J. Phys. Soc. Jpn. **83**, 094001 (2014).
[60] R. Steinigeweg, J. Gemmer, and W. Brenig, Phys. Rev. Lett. **112**, 120601 (2014).
[61] A. Klümper and K. Sakai, J. Phys. A **35**, 2173 (2002).
[62] X. Zotos, Phys. Rev. Lett. **92**, 067202 (2004).
[63] P. Jung, R. W. Helmes, and A. Rosch, Phys. Rev. Lett. **96**, 067202 (2006).
[64] S. Langer, F. Heidrich-Meisner, J. Gemmer, I. P. McCulloch, and U. Schollwöck, Phys. Rev. B **79**, 214409 (2009).
[65] M. Žnidarič, Phys. Rev. B **88**, 205135 (2013).
[66] C. Karrasch, D. Kennes, and F. Heidrich-Meisner, Phys. Rev. B **91**, 115130 (2015).
[67] R. Steinigeweg, J. Herbrych, X. Zotos, and W. Brenig, Phys. Rev. Lett. **116**, 017202 (2016).
[68] S. Nishimoto and M. Arikawa, Phys. Rev. B **79**, 113106 (2009).
[69] A. Metavitsiadis and W. Brenig, Phys. Rev. B **96**, 041115(R) (2017).
[70] M. Žnidarič, Phys. Rev. Lett. **110**, 070602 (2013).
[71] R. Steinigeweg, F. Heidrich-Meisner, J. Gemmer, K. Michielsen, and H. De Raedt, Phys. Rev. B **90**, 094417 (2014).
[72] C. Bartsch and J. Gemmer, Phys. Rev. Lett. **102**, 110403 (2009).
[73] P. Reimann, Phys. Rev. E **97**, 062129 (2018).
[74] K. Fabricius, U. Löw, and J. Stolze, Phys. Rev. B **55**, 5833 (1997).
[75] R. Steinigeweg and J. Gemmer, Phys. Rev. B **80**, 184402 (2009).
[76] For $\varrho_l = S^z_{l,1} + S^z_{l,2}$ we have $\chi = 1/2$, while for $\varrho_l = h_l$ we find $\chi = 3(2J_\parallel^2 + J_\perp^2)/16$.
[77] Note that in the case of energy dynamics, we also find two smaller peaks at adjacent lattice sites $L/2 \pm 1$. This is caused by the fact that $[h_l, h_{l\pm1}] \neq 0$.
[78] R. Steinigeweg, H. Wichterich, and J. Gemmer, EPL (Europhys. Lett.) **88**, 10004 (2009).
[79] Y. Yan, F. Jiang, and H. Zhao, Eur. Phys. J. B **88**, 11 (2015).
[80] H. De Raedt and K. Michielsen, in *Handbook of Theoretical and Computational Nanotechnology* (American Scientific Publishers, Los Angeles, 2006).
[81] V. V. Dobrovitski and H. De Raedt, Phys. Rev. E **67**, 056702 (2003).
[82] A. Weiße, G. Wellein, A. Alvermann, and H. Fehske, Rev. Mod. Phys. **78**, 275 (2006).

[83] V. K. Varma, A. Lerose, F. Pietracaprina, J. Goold, and A. Scardicchio, J. Stat. Mech. (2017) 053101.
[84] J. Richter and R. Steinigeweg, Phys. Rev. E **99**, 012114 (2019).
[85] L. Knipschild and J. Gemmer, Phys. Rev. E **98**, 062103 (2018).
[86] L. Knipschild and J. Gemmer, Phys. Rev. A **99**, 012118 (2019).
[87] J. Herbrych, R. Steinigeweg, and P. Prelovšek, Phys. Rev. B **86**, 115106 (2012).
[88] I. Rousochatzakis, S. Kourtis, J. Knolle, R. Moessner, and N. B. Perkins, arXiv:1811.01671.